Nano Research 2017, 10(7): 2386–2394
DOI 10.1007/s12274-017-1436-3
Research Article
ISSN 1998-0124
CN 11-5974/O4

Synthesis of large-scale atomic-layer SnS_2 through chemical vapor deposition

Gonglan Ye[1], Yongji Gong[2,5] (✉), Sidong Lei[1], Yongmin He[1], Bo Li[1], Xiang Zhang[3], Zehua Jin[1], Liangliang Dong[2], Jun Lou[1], Robert Vajtai[1], Wu Zhou[4], and Pulickel M. Ajayan[1,2] (✉)

[1] *Department of Materials Science & NanoEngineering, Rice University, Houston, Texas 77005, USA*
[2] *Department of Chemistry, Rice University, Houston, Texas 77005, USA*
[3] *Department of Applied Physics, Rice University, Houston, Texas 77005, USA*
[4] *Materials Science & Technology Division, Oak Ridge National Lab, Oak Ridge, TN 37831, USA*
[5] *School of Materials Science and Engineering, Beihang University, Beijing 100191, China*

Received: 23 September 2016
Revised: 21 December 2016
Accepted: 26 December 2016

KEYWORDS
metal dichalcogenides,
tin disulfide,
two-dimensional materials,
chemical vapor deposition,
photodetector

ABSTRACT

Two-dimensional layers of metal dichalcogenides have attracted much attention because of their ultrathin thickness and potential applications in electronics and optoelectronics. Monolayer SnS_2, with a band gap of ~2.6 eV, has an octahedral lattice made of two atomic layers of sulfur and one atomic layer of tin. Till date, there have been limited reports on the growth of large-scale and high quality SnS_2 atomic layers and the investigation of their properties as a semiconductor. Here, we report the chemical vapor deposition (CVD) growth of atomic-layer SnS_2 with a large crystal size and uniformity. In addition, the number of layers can be changed from a monolayer to few layers and to bulk by changing the growth time. Scanning transmission electron microscopy was used to analyze the atomic structure and demonstrate the 2H stacking poly-type of different layers. The resultant SnS_2 crystals is used as a photodetector with external quantum efficiency as high as 150%, suggesting promise for optoelectronic applications.

1 Introduction

Two-dimensional layered metal dichalcogenides (LMDs) such as MoS_2 [1–5] and WS_2 [6] have attracted great attention because of their potential applications in areas such as optics, electronics, and catalysis [3, 7–16]. For example, thinning down some 2D LMD materials such as MoS_2 and $MoSe_2$ [17, 18] from bulk to monolayer leads to new phenomena such as indirect to a direct band gap transition and results in significant enhancement of photosensitivity [19–23]. MoS_2 has already been extensively studied due to its appealing optical and electronic properties. However, the investigation of 2D LMD SnS_2 is still in its nascent stage. Monolayer SnS_2 has the $P\bar{3}m1$ space group, where the Sn ions are coordinated by six S ions with a 1T polymorph structure [24–26]. Unlike MoS_2, SnS_2 has an indirect bandgap for both monolayer and bulk crystals.

Address correspondence to Yongji Gong, yongjigong@buaa.edu.cn; Pulickel M. Ajayan, ajayan@rice.edu

Its band gap ranges from 2.0 to 2.6 eV, as shown by both experimental and theoretical data, which is significantly larger than that for MoS_2. However, the relationship between the bandgap of SnS_2 and the number of layers is still unclear yet [27–30]. The benefit of the larger band gap of SnS_2 is that field effect transistors (FETs) based on this compound could have larger on/off current ratios and lower off-state leakage currents [31, 32]. More importantly, the wide band gap, which is larger than that of any other reported LMD, permits devices to operate at much higher voltages, frequencies, and temperatures, thus reducing operation costs and increasing the energy efficiency. Most studies on SnS_2 in the literature are focused on applications related to energy storage and conversion, such as lithium ion batteries and water splitting [33–36]. Until now, there are only a few reports on the growth and electrical and optical properties of atomically thin SnS_2 layers. Notably, recent studies have shown that monolayer SnS_2 is competitive and promising for electrical and optical devices, with a mobility of 50 $cm^2 \cdot V^{-1} \cdot s^{-1}$ as field-effect transistors [37] and a fast photocurrent response [19, 38–40].

Further efforts are required for the synthesis of high-quality, large-scale atomic-layer SnS_2 [38, 41]. Similar to other 2D layered materials such as graphene, MoS_2 and WS_2, exfoliation of bulk SnS_2 is a simple and effective way to obtain the corresponding monolayers [42]. However, the exfoliated SnS_2 has limited applications due to poor control over thickness and size. Besides exfoliation, chemical vapor deposition (CVD) [37], hydrothermal methods [24], and spin coating techniques [43] have also been developed to produce atomic layer SnS_2. Among them, CVD is known to be the most successful method for the synthesis of various large-scale atomic layer 2D materials such as MoS_2, $MoSe_2$, and their heterostructures [44, 45]. Although some success has been achieved using CVD for growing SnS_2 atomic layers, there are challenges such as limitation in size and difficulty in controlling the number of layers down to the monolayer [38]. Thus, further improvement is necessary to obtain large-scale and high quality SnS_2 with a controlled number of layers for practical applications [38, 39].

Here, we report a facile and scalable CVD method to synthesize large-size and high-quality SnS_2 atomic layers. The edge of the single-crystal domains can be as long as 128 μm and the layer numbers can be controlled from monolayer to bulk. The Raman peak position shift and intensity change are observed as a function of the number of layers. Atomic resolution scanning transmission electron microscopy (STEM) was further used to show the high-quality lattice of SnS_2 with 2H stacking between different layers (Sn aligned with Sn, and S aligned with S). Finally, photodetectors based on the CVD grown SnS_2 were fabricated with a high external quantum efficiency of 150% and an on/off ratio as high as 10^2, suggesting the potential applicability of SnS_2 in photodetectors and sensors.

2 Results and discussion

SnS_2 was grown by using tin oxalate (SnC_2O_4) and sulfur as the Sn and S precursors, respectively. A clean Si wafer with 275 nm SiO_2 was used as the substrate located at the center of the furnace (Fig. 1(a)). 100 sccm Ar was used as the carrier gas and to create an inert atmosphere during the growth procedure, including the heating and cooling processes. The S powder was placed in another porcelain boat and located upstream in a lower temperature zone. The furnace was ramped up from room temperature to 600 °C over 15 min and maintained at this temperature for 5–10 min for the growth. Finally, the furnace was allowed to cool naturally. Compared to other Sn sources (Sn and SnO_2), SnC_2O_4 has medium vapor pressure at the reaction temperature (600 °C), which is beneficial for the reaction. The reaction process during CVD growth should be

$$SnC_2O_4 \rightarrow SnO + CO + CO_2 \quad (1)$$

$$2SnO + 5S \rightarrow 2SnS_2 + SO_2 \quad (2)$$

Figure 1(b) shows a low-magnification optical image of the as-grown SnS_2. High-coverage SnS_2 triangles and hexagons with atomic thickness and uniform size were formed after growth. The general size of the SnS_2 crystals ranges from tens of micrometers to more than a hundred micrometers (Figs. 1(b)–1(e)), and the largest crystal is about 128 μm in edge. The resultant atomic layers of SnS_2 were also characterized by a scanning electron microscope (Fig. S1 in Electronic Supple-

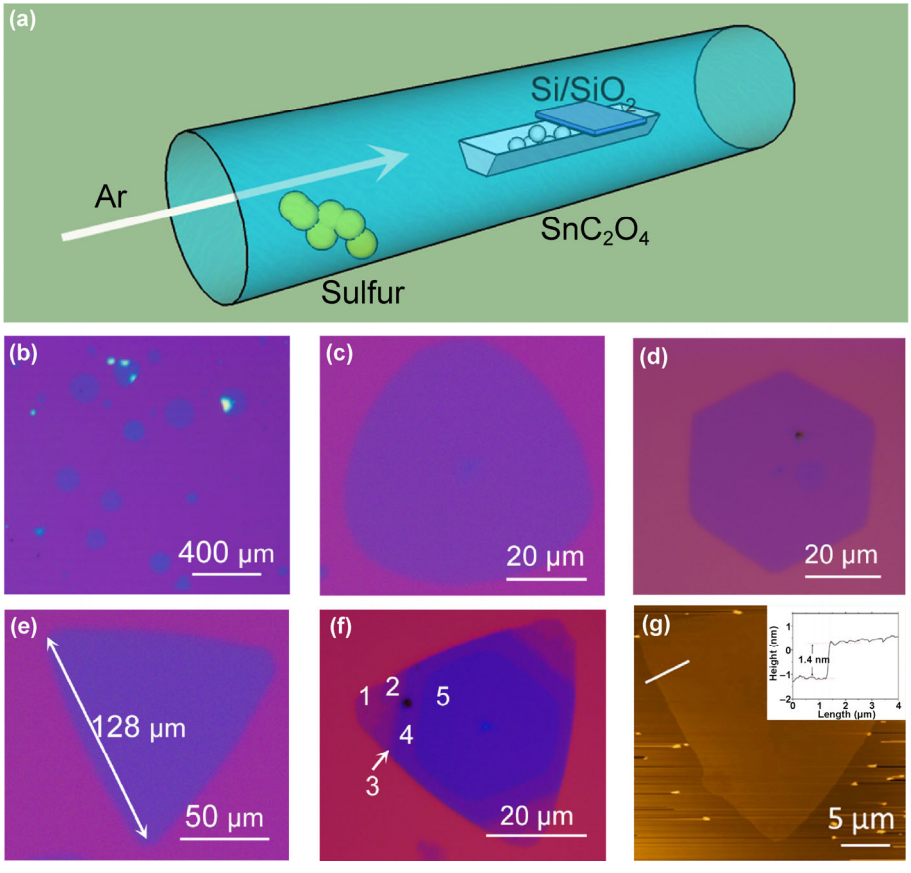

Figure 1 Synthesis and morphology of atomic-layer SnS_2. (a) Schematic of the synthesis of SnS_2 by CVD, where sulfur and tin oxalate are used as the precursors. (b) Large-scale image to show the high yield of SnS_2 atomic layers. ((c)–(e)) Typical optical images of SnS_2 single crystals with round triangle, hexagon, and sharp triangle shapes, respectively. The edge of the SnS_2 single crystals can be as long as 128 μm. (f) Optical image showing a multilayer SnS_2 single crystal, which consists of a monolayer in the edge region and a five-layer region at the center (the layer numbers are marked out). (g) AFM image of a resultant SnS_2 single crystal. The height profile (inset) shows a thickness of 1.4 nm, illustrating that the tested SnS_2 single crystal is bilayer.

mentary Material (ESM)). The large size of the SnS_2 single crystals can facilitate device fabrication and corresponding characterizations. Notably, most of the SnS_2 single crystals do not exhibit sharp angels and straight edges, which are significantly different from the CVD grown MoS_2. Similar to other 2D materials, the thickness and the number of layers of the resultant SnS_2 can be easily distinguished via optical images owing to their optical contrast [25]. Clearly, the bright yellow regions in Fig. 1(b) indicate thick SnS_2 crystals (bulk), while the atomic layers appear blue in color. Figure 1(f) shows a 5-layer SnS_2 single crystal, where the layer number is marked in the figure. In addition, we can roughly tune the sample thickness by adjusting the growth time. For example, 5 min growth will yield samples dominated by 1–5 layers in thickness, as shown in Figs. 1(b)–1(f), while bulk crystals become dominant with 10 min growth (Fig. S2 in ESM). The thickness of the as-grown SnS_2 was measured by atomic force microscopy (AFM). As shown in Fig. 1(g), the measured sample, which has uniform thickness and a clean surface, shows a thickness of 1.4 nm, corresponding to a bilayer SnS_2 crystal [38]. Monolayer SnS_2 crystals with a thickness of 0.87 nm were characterized by AFM (Fig. S3 in the ESM).

Raman spectroscopy is an effective technique to identify the crystal quality and the number of layers of 2D materials [46]. Figure 2(a) shows an optical image of a multilayer SnS_2 single crystal with an edge around 30 μm, characterized by a 514.5 nm laser. From

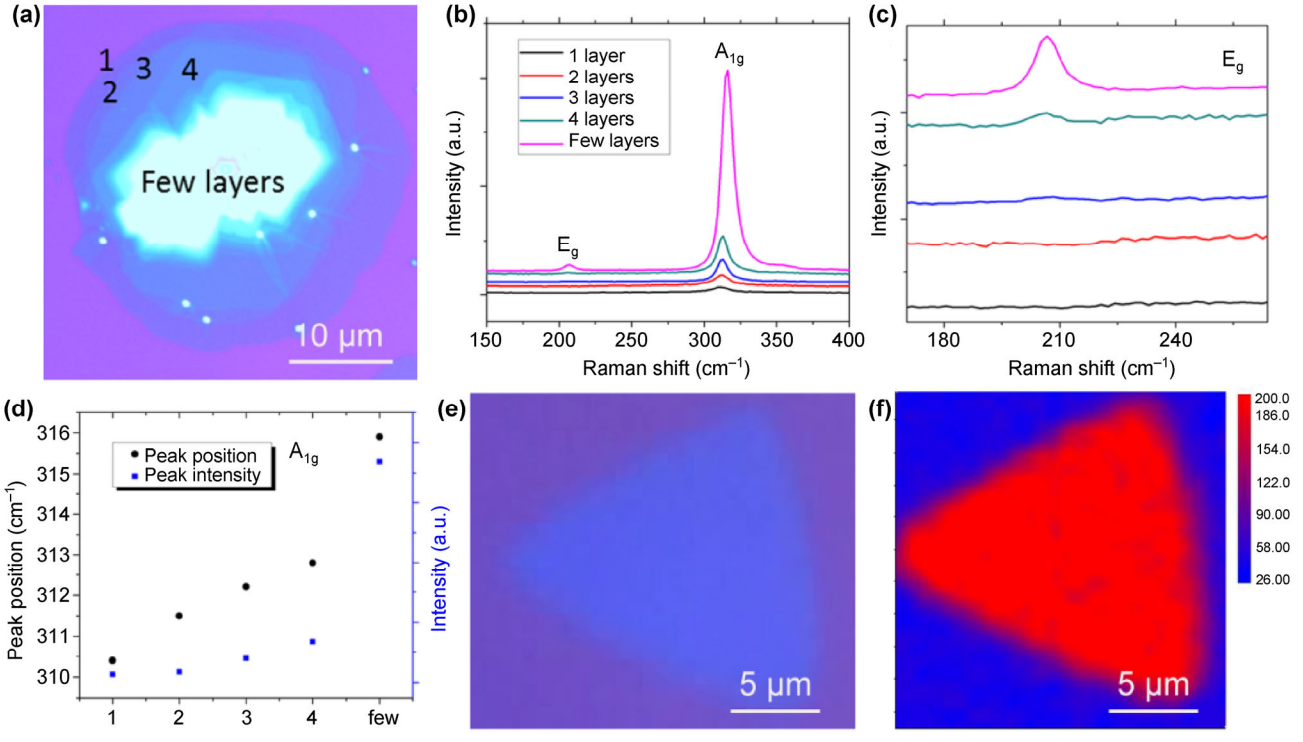

Figure 2 Raman characterization of the resultant SnS_2. (a) Optical image of a multilayer SnS_2. (b) Raman spectra of different layered SnS_2 samples marked in (a). Two main characteristic peaks are located at ~317 and ~208 cm^{-1}. (c) Enlarged Raman spectra at the characteristic peak of ~208 cm^{-1}. The E_g peak appears from the 3rd layer as the thickness increased from a monolayer to a few layers. (d) Change in position and intensity of the A_{1g} peak with number of layers. As the number of layers increases, the peak is blue-shifted and the peak intensity increases. (e) Optical image of a triangular SnS_2 single crystal and the corresponding Raman mapping of the A_{1g} mode (f).

the edge to the center, the layer number changes from a monolayer to a few layers. Notably, there are clear steps among the monolayer, bilayer, three layer, and four layer regions, marked as 1, 2, 3, 4, respectively, which are chosen on purpose to study the layer number dependence of Raman spectra. Figure 2(b) shows the Raman spectra of the chosen SnS_2 crystal collected at different layers. The two main peaks at 317 cm^{-1} (A_{1g} phonon mode) and 208 cm^{-1} (E_g phonon mode) are the characteristic peaks of SnS_2. As the thickness increases from monolayer to bulk, the E_g peak appears from the 3rd layer but its intensity is much weaker than that for the few-layer region (Fig. 2(c)). These phenomena match well with previously reported results, which can be attributed to the increase in the number of scattering centers for in-plane scattering [47, 48]. Furthermore, Fig. 2(d) shows the relationship between the A_{1g} peak and the number of layers, where a significant increase in the peak intensity and blueshift of the peak position are observed. Specifically, the peak shifts from 310.4, 311.5, 312.1, to 312.8 cm^{-1} from the monolayer to four-layer samples. These changes provide a feasible method to identify the thickness of the SnS_2 atomic layers. Figures 2(e) and 2(f) show an optical image of a triangular SnS_2 single crystal and its corresponding Raman intensity map at 317 cm^{-1}. The uniform Raman intensity in the map indicates highly homogeneous and uniform SnS_2 atomic layers. Because of the indirect and wide band gap of SnS_2, it is difficult to examine its band gap by photoluminescence.

Z contrast imaging (*Z* is the atomic number) from an aberration-corrected STEM was used to further demonstrate the high crystal quality of the CVD grown SnS_2 at the atomic level. Since the image intensity is directly related to the averaged atomic number and the thickness of the sample, *Z* contrast imaging can be used to quantify the number of layers [49]. By using the poly(methyl methacrylate) (PMMA) assisted transfer technique, the resultant SnS_2 sample can be transferred onto a TEM grid. Figures 3(a) and 3(b) depict the low-

magnification Z contrast images of the resultant SnS_2. In Fig. 3(a), the dark area represents a bilayer region, while the bright part is a trilayer area [49]. Figure 3(b) shows the bi-, tri-, and four-layer SnS_2, with the corresponding thickness labeled in the image. The small particles and narrow cracks observed in Figs. 3(a) and 3(b) were caused by the transfer process [17]. In atomic resolution high-angle annular dark field (HAADF) (Fig. 3(c)) and bright field images (Fig. S4(a) in the ESM) and the deconvolved HAADF image (Fig. 3(d)) of the bilayer SnS_2, the intensity ratio between the bright and dark columns corresponds to the ratio between 2 overlapped Sn atoms (bright columns) and 2 S atoms at each less intense columns [50]. Considering the 1T phase of monolayer SnS_2 (octahedral), this bilayer structure should be a 2H stacking polytype of the two monolayers [25], where tin and sulfur in one layer aligned with tin and sulfur in the other layer, similar to a bulk crystal. The electron energy loss spectroscopy (EELS) analysis of the crystal illustrates the presence of S and Sn (Fig. S4(b) in the ESM). The diffraction pattern constructed from fast Fourier transform (FFT) in the inset of Fig. 3(c) shows the hexagonal structure. Furthermore, four-layer and seven-layer SnS_2 samples are characterized by STEM. As shown in Fig. 3(e), the STEM image of four-layer SnS_2 shows similar hexagonal lattice to the bilayer one. The patches with slightly different contrast are caused by the sample damage under electron beam illumination. In comparison, seven-layer SnS_2 is much more stable upon exposure to the electron beam. As shown in Fig. 3(f), the STEM image together with the FFT pattern shows the hexagonal structure of SnS_2 with a uniform contrast. The elemental composition of the CVD grown SnS_2 crystal is determined by X-ray photoelectron spectroscopy (XPS) (Fig. S5 in the ESM). From high-resolution XPS, the ratio of Sn/S is found to be ~1:1.98, suggesting reasonably stoichiometric composition of the CVD grown SnS_2.

To further illustrate the potential application of SnS_2, a two-terminal device was fabricated on single-layered SnS_2 with a Au/Ti (Au 38 nm/Ti 2 nm) electrode by e-beam lithography. The channel length and width were 2 μm and about 20 μm, respectively (Fig. 4(a)).

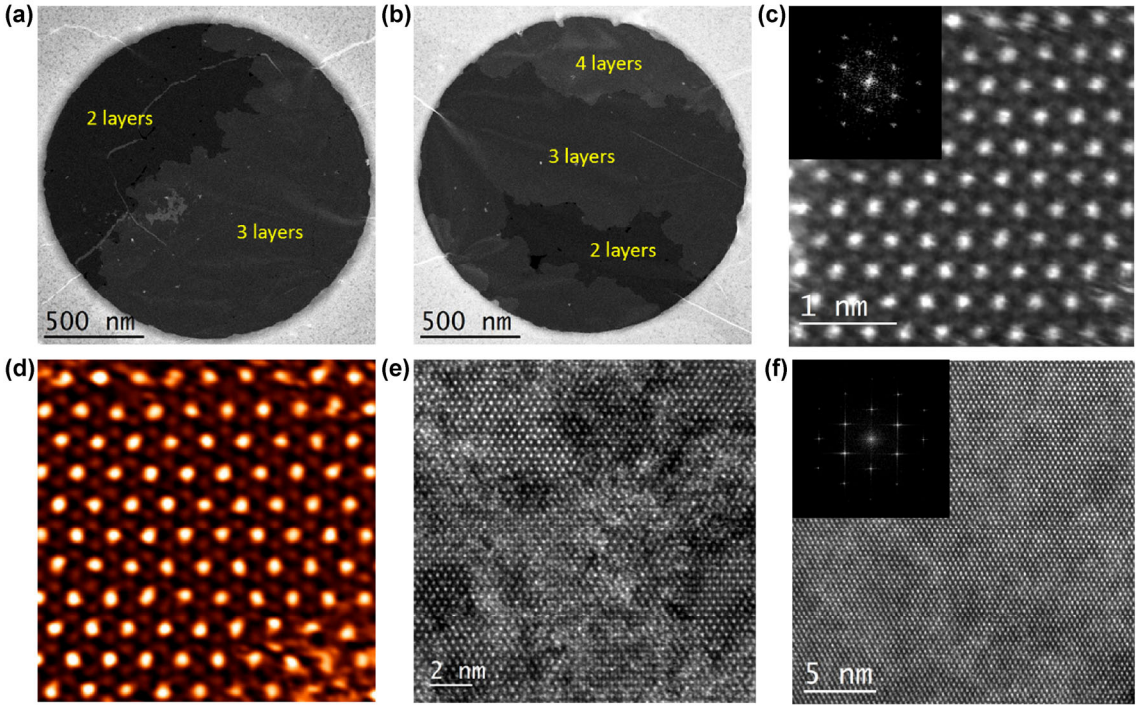

Figure 3 STEM characterization of SnS_2 atomic layers. (a) and (b) SnS_2 samples with different numbers of layers, where the thickness is quantified via averaged ADF imaging intensity. (c) STEM ADF image and (d) deconvolved ADF image of bilayer SnS_2 show its perfect hexagonal lattice, as confirmed by the corresponding FFT in the inset. ((e) and (f)) STEM ADF images of four-layer (e) and seven-layer SnS_2 samples (f). Inset in (f) shows the corresponding FFT pattern, revealing the hexagonal structure and high crystal quality.

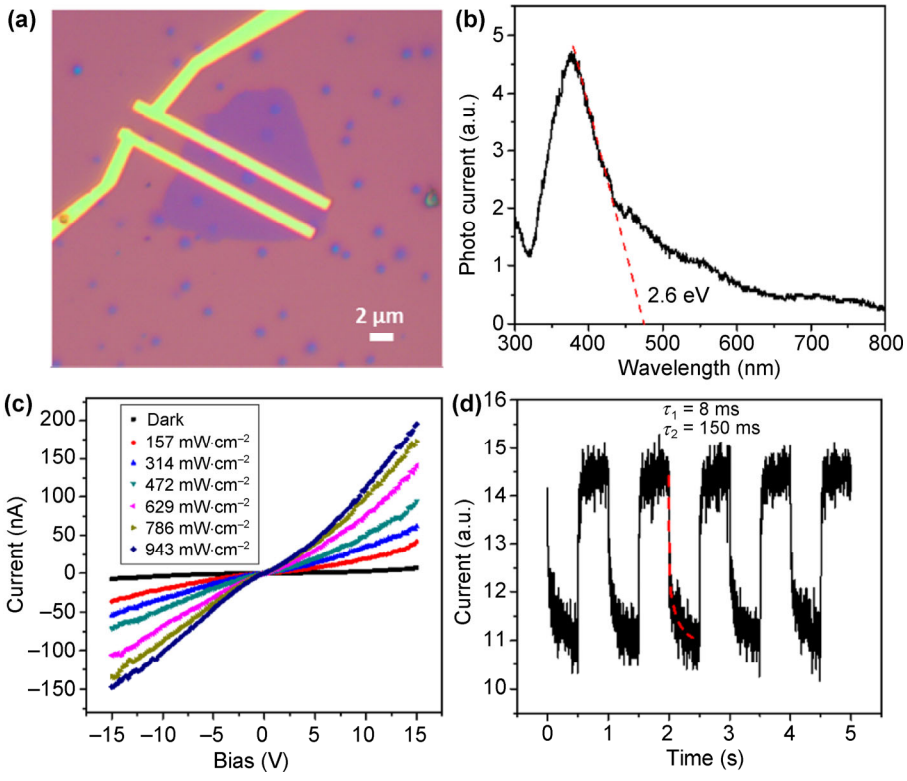

Figure 4 Photodetection of a monolayer SnS_2 device. (a) Optical image of the fabricated device. (b) Photoconductivity spectrum of monolayer SnS_2 showing the strongest photoconductivity at about 390 nm with an estimated band gap of 2.6 eV. (c) *IV* curve of the SnS_2 device with different illumination powers. The non-linearity of the curve indicates the existence of a Schottky barrier between the electrodes and SnS_2. (d) The response speed of the resultant SnS_2.

Photoconductivity was performed on this device. Figure 4(b) shows the photoconductivity spectrum of the single-layered SnS_2. Monolayer SnS_2 showed the strongest photoconductivity with 390 nm light and the band gap of single-layered SnS_2 was determined to be about 2.6 eV. There is an obvious tail in the photoconductivity spectrum extending to about 650 nm. There might be two aspects contributing to this tail. First, the Schottky barrier between the Au/Ti electrodes and SnS_2 can lead to electron excitation from the metal Fermi surface to the conduction band of SnS_2. The other important aspect is the excitation from the energy levels inside the SnS_2 bandgap. These energy levels always serve as charge carrier trap states, which can lead to very high external quantum efficiency but longer response time, as discussed below [51]. Figure 4(c) shows the photoconductivity *IV* curve of the SnS_2 device. The *IV* curve does not show linearity, which indicates the existence of a Schottky barrier between the electrodes and SnS_2. As the bias voltage increases, the photocurrent increases. With a 15 V bias, the external quantum efficiency can be as high as 150%, because of the existence of trap states. It is noteworthy that the photoconductivity response is from monolayer SnS_2 rather than the 10 nm SnS_2 from Ref. [38], which might result in very different performances. After the photoexcitation, electrons are injected into conduction band and holes are left in the valence band; both the electrons and holes take part in the photoconductivity process. However, if one kind of charge carriers would be trapped at the trapping center, for example, if holes are trapped near the valence band, the electrons will stay in the conduction band for a longer time before combining with the holes. This effect leads to effective n-type doping and makes SnS_2 more conductive, yielding an external quantum efficiency of more than 100%. The other evidence for this trap state is the relatively low response speed, as demonstrated in Fig. 4(d). By fitting the falling edge of the modulated photocurrent, two time components

can be found, a fast component of 8 ms and a slow component of 150 ms. The slow response component is strong evidence for the existence of the trap states. The external quantum efficiency is higher than that in a previous report [38], and the response time is longer. These two factors together indicate the existence of trap states, which may result from the interface conditions between SnS_2 and SiO_2. We also measured the FET performance of the resultant monolayer SnS_2, as shown in Figs. S6 and S7 in the ESM.

3 Conclusion

In conclusion, we report a facile CVD method to synthesize 2D atomic-layer SnS_2. The size of the resultant SnS_2 single crystal domains can be as large as 128 μm and thinned down to monolayer and bilayer. An external quantum efficiency of 150% can be achieved as a photodetector, promising for electronic and optoelectronic applications. More importantly, the wide bandgap of SnS_2 opens up more opportunities for the applications of 2D materials.

4 Experimental section

4.1 Growth of atomic layers SnS_2 via CVD

Sulfur (99.5%, Sigma-Aldrich) powder and tin oxalate (SnC_2O_4) powder were used as the S and Sn precursors, respectively. S was placed in an alumina boat at the upstream, where the temperature was lower, which was around 200 ˚C during growth. Another boat with the Sn precursor and a top face down Si/SiO_2 substrate was placed at the center of the quartz tube (the hot zone). The temperature program was set as follows: ramping up from room temperature to 600 ˚C in 15 min, then 600 ˚C for 5–10 min, and cooling to room temperature naturally. 100 sccm Ar was used during the entire process. The growth was affected under atmospheric pressure.

4.2 TEM sample preparation

The TEM samples were prepared by using a poly(methyl methacrylate) (PMMA) assisted transfer technique. First, the $SnS_2/SiO_2/Si$ substrate was spin-coated by a PMMA film (3,500 rpm for 40 s). Then, SiO_2 was etched by 2 M KOH solution, and the PMMA/SnS_2 was subjected to a lift-off process. Subsequently, the PMMA/SnS_2 was transferred onto the TEM grid and dried naturally. Finally, PMMA was washed away by acetone and 2-propanol.

Acknowledgements

This work was supported by the Army Research Office MURI (No. W911NF-11-1-0362), the FAME Center, one of six centers of STARnet, a Semiconductor Research Corporation program sponsored by MARCO and DARPA. This research was supported in part by the U.S. Department of Energy, Office of Science, Basic Energy Science, Materials Sciences and Engineering Division (WZ), and through a user project conducted at the Center for Nanophase Materials Sciences, which is a DOE Office of Science User Facility.

Electronic Supplementary Material: Supplementary material (the morphology characterization of SnS_2 atomic layers, AFM images, TEM images, and XPS characterization) is available in the online version of this article at http://dx.doi.org/10.1007/s12274-017-1436-3.

References

[1] Kim, K. S.; Zhao, Y.; Jang, H.; Lee, S. Y.; Kim, J. M.; Kim, K. S.; Ahn, J.-H.; Kim, P.; Choi, J.-Y.; Hong, B. H. Large-scale pattern growth of graphene films for stretchable transparent electrodes. *Nature* **2009**, *457*, 706–710.

[2] Lee, Y. H.; Zhang, X. Q.; Zhang, W. J.; Chang, M.-T.; Lin, C.-T.; Chang, K.-D.; Yu, Y.-C.; Wang, J. T.-W.; Chang, C.-S.; Li, L.-J. et al. Synthesis of large-area MoS_2 atomic layers with chemical vapor deposition. *Adv. Mater.* **2012**, *24*, 2320–2325.

[3] Li, H.; Wu, J.; Huang, X.; Yin, Z. Y.; Liu, J. Q.; Zhang, H. A universal, rapid method for clean transfer of nanostructures onto various substrates. *ACS Nano* **2014**, *8*, 6563–6570.

[4] Li, H.; Yin, Z. Y.; He, Q. Y.; Li, H.; Huang, X.; Lu, G.; Fam, D. W. H.; Tok, A. I. Y.; Zhang, Q.; Zhang, H. Fabrication of single- and multilayer MoS_2 film-based field-effect transistors for sensing NO at room temperature. *Small* **2012**, *8*, 63–67.

[5] Zeng, Z. Y.; Yin, Z. Y.; Huang, X.; Li, H.; He, Q. Y.; Lu, G.; Boey, F.; Zhang, H. Single-layer semiconducting nanosheets: High-yield preparation and device fabrication.

Angew. Chem., Int. Ed. **2011**, *50*, 11093–11097.

[6] Cong, C. X.; Shang, J. Z.; Wu, X.; Cao, B. C.; Peimyoo, N.; Qiu, C. Y.; Sun, L. T.; Yu, T. Synthesis and optical properties of large-area single-crystalline 2D semiconductor WS_2 monolayer from chemical vapor deposition. *Adv. Opt. Mater*. **2014**, *2*, 131–136.

[7] Okada, M.; Sawazaki, T.; Watanabe, K.; Taniguch, T.; Hibino, H.; Shinohara, H.; Kitaura, R. Direct chemical vapor deposition growth of WS_2 atomic layers on hexagonal boron nitride. *ACS Nano* **2014**, *8*, 8273–8277.

[8] Feng, Q. L.; Zhu, Y. M.; Hong, J. H.; Zhang, M.; Duan, W. J.; Mao, N. N.; Wu, J. X.; Xu, H.; Dong, F. L.; Lin, F. et al. Growth of large-area 2D $MoS_{2(1-x)}Se_{2x}$ semiconductor alloys. *Adv. Mater*. **2014**, *26*, 2648–2653.

[9] Chang, Y. H.; Zhang, W. J.; Zhu, Y. H.; Han, Y.; Pu, J.; Chang, J.-K.; Hsu, W.-T.; Huang, J.-K.; Hsu, C.-L.; Chiu, M.-H. et al. Monolayer $MoSe_2$ grown by chemical vapor deposition for fast photodetection. *ACS Nano* **2014**, *8*, 8582–8590.

[10] Chen, J. Z.; Wu, X. J.; Yin, L. S.; Li, B.; Hong, X.; Fan, Z. X.; Chen, B.; Xue, C.; Zhang, H. One-pot synthesis of CdS nanocrystals hybridized with single-layer transition-metal dichalcogenide nanosheets for efficient photocatalytic hydrogen evolution. *Angew. Chem., Int. Ed*. **2015**, *54*, 1210–1214.

[11] Tan, C. L.; Zhang, H. Two-dimensional transition metal dichalcogenide nanosheet-based composites. *Chem. Soc. Rev*. **2015**, *44*, 2713–2731.

[12] Zhang, H. Ultrathin two-dimensional nanomaterials. *ACS Nano* **2015**, *9*, 9451–9469.

[13] Lu, Q. P.; Yu, Y. F.; Ma, Q. L.; Chen, B.; Zhang, H. 2D transition-metal-dichalcogenide-nanosheet-based composites for photocatalytic and electrocatalytic hydrogen evolution reactions. *Adv. Mater*. **2016**, *28*, 1917–1933.

[14] Huang, X.; Zeng, Z. Y.; Bao, S. Y.; Wang, M. F.; Qi, X. Y.; Fan, Z. X.; Zhang, H. Solution-phase epitaxial growth of noble metal nanostructures on dispersible single-layer molybdenum disulfide nanosheets. *Nat. Commun*. **2013**, *4*, 1444.

[15] Yin, Z. Y.; Chen, B.; Bosman, M.; Cao, X. H.; Chen, J. Z.; Zheng, B.; Zhang, H. Au nanoparticle-modified MoS_2 nanosheet-based photoelectrochemical cells for water splitting. *Small* **2014**, *10*, 3537–3543.

[16] Ma, C. B.; Qi, X. Y.; Chen, B.; Bao, S. Y.; Yin, Z. Y.; Wu, X.-J.; Luo, Z. M.; Wei, J.; Zhang, H.-L.; Zhang, H. MoS_2 nanoflower-decorated reduced graphene oxide paper for high-performance hydrogen evolution reaction. *Nanoscale* **2014**, *6*, 5624–5629.

[17] Wang, X. L.; Gong, Y. J.; Shi, G.; Chow, W. L.; Keyshar, K.; Ye, G. L.; Vajtai, R.; Lou, J.; Liu, Z.; Ringe, E. et al. Chemical vapor deposition growth of crystalline monolayer $MoSe_2$. *ACS Nano* **2014**, *8*, 5125–5131.

[18] Wu, J.; Li, H.; Yin, Z. Y.; Li, H.; Liu, J. Q.; Cao, X. H.; Zhang, Q.; Zhang, H. Layer thinning and etching of mechanically exfoliated MoS_2 nanosheets by thermal annealing in air. *Small* **2013**, *9*, 3314–3319.

[19] Xia, J.; Huang, X.; Liu, L. Z.; Wang, M.; Wang, L.; Huang, B.; Zhu, D.-D.; Li, J.-J.; Gu, C.-Z.; Meng, X.-M. CVD synthesis of large-area, highly crystalline $MoSe_2$ atomic layers on diverse substrates and application to photodetectors. *Nanoscale* **2014**, *6*, 8949–8955.

[20] Schmidt, H.; Wang, S. F.; Chu, L. Q.; Toh, M.; Kumar, R.; Zhao, W. J.; Castro Neto, A. H..; Martin, J.; Adam, S.; Özyilmaz, B. et al. Transport properties of monolayer MoS_2 grown by chemical vapor deposition. *Nano Lett*. **2014**, *14*, 1909–1913.

[21] Lu, X.; Utama, M. I. B.; Lin, J. H.; Gong, X.; Zhang, J.; Zhao, Y. Y.; Pantelides, S T.; Wang, J. X.; Dong, Z. L.; Liu, Z. et al. Large-area synthesis of monolayer and few-layer $MoSe_2$ films on SiO_2 substrates. *Nano Lett*. **2014**, *14*, 2419–2425.

[22] Keyshar, K.; Gong, Y. J.; Ye, G. L.; Brunetto, G.; Zhou, W.; Cole, D. P.; Hackenberg, K.; He, Y. M.; Machado, L.; Kabbani, M. et al. Chemical vapor deposition of monolayer rhenium disulfide (ReS_2). *Adv. Mater*. **2015**, *27*, 4640–4648.

[23] Koski, K. J.; Cui, Y. The new skinny in two-dimensional nanomaterials. *ACS Nano* **2013**, *7*, 3739–3742.

[24] Feng, J. J.; Chen, J. T.; Geng, B. S.; Feng, H. T.; Li, H. J.; Yan, D.; Zhuo, R. F.; Cheng, S.; Wu, Z. G.; Yan, P. X. Two-dimensional hexagonal SnS_2 nanoflakes: Fabrication, characterization, and growth mechanism. *Appl. Phys. A* **2011**, *103*, 413–419.

[25] Seminovski, Y.; Palacios, P.; Wahnón, P. Effect of van der Waals interaction on the properties of SnS_2 layered semiconductor. *Thin Solid Films* **2013**, *535*, 387–389.

[26] Kappera, R.; Voiry, D.; Yalcin, S. E.; Branch, B.; Gupta, G.; Mohite, A. D.; Chhowalla, M. Phase-engineered low-resistance contacts for ultrathin MoS_2 transistors. *Nat. Mater*. **2014**, *13*, 1128–1134.

[27] He, X. C.; Shen, H. L. *Ab initio* calculations of band structure and thermophysical properties for SnS_2 and $SnSe_2$. *Phys. B: Condens. Matter* **2012**, *407*, 1146–1152.

[28] Huang, Y.; Sutter, E.; Sadowski, J. T.; Cotlet, M.; Monti, O. L. A.; Racke, D. A.; Neupane, M. R.; Wickramaratne, D.; Lake, R. K.; Parkinson, B. A. et al. Tin disulfide—An emerging layered metal dichalcogenide semiconductor: Materials properties and device characteristics. *ACS Nano* **2014**, *8*, 10743–10755.

[29] Liu, Z. X.; Deng, H. Q.; Mukherjee, P. P. Evaluating pristine and modified SnS_2 as a lithium-ion battery anode: A first-principles study. *ACS Appl. Mater. Interfaces* **2015**, *7*, 4000–4009.

[30] Zhuang, H. L.; Hennig, R. G. Theoretical perspective of photocatalytic properties of single-layer SnS_2. *Phys. Rev. B* **2013**, *88*, 115314.

[31] Joshi, P. D.; Joag, D. S.; Rout, C. S.; Late, D. J. Photosensitive field emission study of SnS_2 nanosheets. In *Proceedings of the 2014 27th International Vacuum Nanoelectronics Conference*, Engelberg, 2014, pp 241–242.

[32] Nørby, P.; Johnsen, S.; Iversen, B. B. Fine tunable aqueous solution synthesis of textured flexible SnS_2 thin films and nanosheets. *Phys. Chem. Chem. Phys.* **2015**, *17*, 9282–9287.

[33] Chang, K.; Wang, Z.; Huang, G. C.; Li, H.; Chen, W. X.; Lee, J. Y. Few-layer SnS_2/graphene hybrid with exceptional electrochemical performance as lithium-ion battery anode. *J. Power Sources* **2012**, *201*, 259–266.

[34] Qu, B. H.; Ma, C. Z.; Ji, G.; Xu, C. H.; Xu, J.; Meng, Y. S.; Wang, T. H.; Lee, J. Y. Layered SnS_2-reduced graphene oxide composite—A high-capacity, high-rate, and long-cycle life sodium-ion battery anode material. *Adv. Mater.* **2014**, *26*, 3854–3859.

[35] Wahnón, P.; Conesa, J. C.; Palacios, P.; Lucena, R.; Aguilera, I.; Seminovski, Y.; Fresno, F. V-doped SnS_2: A new intermediate band material for a better use of the solar spectrum. *Phys. Chem. Chem. Phys.* **2011**, *13*, 20401–20407.

[36] Zhong, H. X.; Yang, G. Z.; Song, H. W.; Liao, Q. Y.; Cui, H.; Shen, P. K.; Wang, C.-X. Vertically aligned graphene-like SnS_2 ultrathin nanosheet arrays: Excellent energy storage, catalysis, photoconduction, and field-emitting performances. *J. Phys. Chem. C* **2012**, *116*, 9319–9326.

[37] Song, H. S.; Li, S. L.; Gao, L.; Xu, Y.; Ueno, K.; Tang, J.; Cheng, Y. B.; Tsukagoshi, K. High-performance top-gated monolayer SnS_2 field-effect transistors and their integrated logic circuits. *Nanoscale* **2013**, *5*, 9666–9670.

[38] Su, G. X.; Hadjiev, V. G.; Loya, P. E.; Zhang, J.; Lei, S. D.; Maharjan, S.; Dong, P.; Ajayan, P. M.; Lou, J.; Peng, H. B. Chemical vapor deposition of thin crystals of layered semiconductor SnS_2 for fast photodetection application. *Nano Lett.* **2015**, *15*, 506–513.

[39] Wen, S. J.; Pan, H.; Zheng, Y. B. Electronic properties of tin dichalcogenide monolayers and effects of hydrogenation and tension. *J. Mater. Chem. C* **2015**, *3*, 3714–3721.

[40] Zschieschang, U.; Holzmann, T.; Kuhn, A.; Aghamohammadi, M.; Lotsch, B. V.; Klauk, H. Threshold-voltage control and enhancement-mode characteristics in multilayer tin disulfide field-effect transistors by gate-oxide passivation with an alkylphosphonic acid self-assembled monolayer. *J. Appl. Phys.* **2015**, *117*, 104509.

[41] Shibata, T.; Miura, T.; Kishi, T.; Nagai, T. Synthesis of single crystal SnS_2 by chemical vapor transport method at low temperature using reverse temperature gradient. *J. Cryst. Growth* **1990**, *106*, 593–604.

[42] Liu, Y. C.; Kang, H. Y.; Jiao, L. F.; Chen, C. C.; Cao, K. Z.; Wang, Y. J.; Yuan, H. T. Exfoliated-SnS_2 restacked on graphene as a high-capacity, high-rate, and long-cycle life anode for sodium ion batteries. *Nanoscale* **2015**, *7*, 1325–1332.

[43] Řičica, T.; Střižík, L.; Dostál, L.; Bouška, M.; Vlček, M.; Beneš, L.; Wágner, T.; Jambor, R. SnS and SnS_2 thin films deposited using a spin-coating technique from intramolecularly coordinated organotin sulfides. *Appl. Organomet. Chem.* **2015**, *29*, 176–180.

[44] Gong, Y. J.; Lei, S. D.; Ye, G. L.; Li, B.; He, Y. M.; Keyshar, K.; Zhang, X.; Wang, Q. Z.; Lou, J.; Liu, Z. et al. Two-step growth of two-dimensional WSe_2/$MoSe_2$ heterostructures. *Nano Lett.* **2015**, *15*, 6135–6141.

[45] Gong, Y. J.; Lin, J. H.; Wang, X. L.; Shi, G.; Lei, S. D.; Lin, Z.; Zou, X. L.; Ye, G. L.; Vajtai, R.; Yakobson, B. I. et al. Vertical and in-plane heterostructures from WS_2/MoS_2 monolayers. *Nat. Mater.* **2014**, *13*, 1135–1142.

[46] Bhatt, S. V.; Deshpande, M. P.; Sathe, V.; Chaki, S. H. Effect of pressure and temperature on Raman scattering and an anharmonicity study of tin dichalcogenide single crystals. *Solid State Commun.* **2015**, *201*, 54–58.

[47] Ahn, J. H.; Lee, M. J.; Heo, H.; Sung, J. H.; Kim, K.; Hwang, H.; Jo, M.-H. Deterministic two-dimensional polymorphism growth of hexagonal n-type SnS_2 and orthorhombic p-type SnS crystals. *Nano Lett.* **2015**, *15*, 3703–3708.

[48] De Groot, C. H.; Gurnani, C.; Hector, A. L.; Huang, R. M.; Jura, M.; Levason, W.; Reid, G. Highly selective chemical vapor deposition of tin diselenide thin films onto patterned substrates via single source diselenoether precursors. *Chem. Mater.* **2012**, *24*, 4442–4449.

[49] Zhou, W.; Zou, X. L.; Najmaei, S.; Liu, Z.; Shi, Y. M.; Kong, J.; Lou, J.; Ajayan, P. M.; Yakobson, B. I.; Idrobo, J.-C. Intrinsic structural defects in monolayer molybdenum disulfide. *Nano Lett.* **2013**, *13*, 2615–2622.

[50] Krivanek, O. L.; Chisholm, M. F.; Nicolosi, V.; Pennycook, T. J.; Corbin, G. J.; Dellby, N.; Murfitt, M. F.; Own, C. S.; Szilagyi, Z. S.; Oxley, M. P. et al. Atom-by-atom structural and chemical analysis by annular dark-field electron microscopy. *Nature* **2010**, *464*, 571–574.

[51] Lei, S. D.; Wen, F. F.; Li, B.; Wang, Q. Z.; Huang, Y. H.; Gong, Y. J.; He, Y. M.; Dong, P.; Bellah, J.; George, A. et al. Optoelectronic memory using two-dimensional materials. *Nano Lett.* **2015**, *15*, 259–265.